electronics

Article

Radar Signal Behavior in Maritime Environments: Falling Rain Effects

Xun Wang [1,2], Menghan Wei [1], Ying Wang [3], Houjun Sun [1] and Jianjun Ma [1,*]

[1] School of Integrated Circuits and Electronics, Beijing Institute of Technology, Beijing 100081, China; 3220185060@bit.edu.cn (X.W.); 3120210675@bit.edu.cn (M.W.); sunhoujun@bit.edu.cn (H.S.)
[2] China Research and Development Academy of Machinery Equipment, Beijing 100089, China
[3] Lenovo (Beijing) Information Technology Corporation Ltd., Beijing 100097, China; wangying47@lenovo.com
[*] Correspondence: jianjun_ma@bit.edu.cn

Abstract: Precision modeling of radar signal behavior in maritime environments holds paramount importance in ensuring the robust functionality of maritime radar systems. This work delves into the intricate dynamics of radar signal propagation in maritime environments, with a particular focus on the effects of falling rain. A theoretical model encompassing raindrop scattering, gaseous absorption, and ocean surface backscattering was developed and validated. Key findings reveal that rain significantly alters radar backscattering, with a noticeable decrease in signal strength under higher rainrates. Additionally, gaseous absorption, particularly at elevated frequencies and humidity levels, emerged as a critical factor. The study also highlights the complex interplay between wind-induced ocean surface roughness and radar signal behavior. We think these insights are pivotal for enhancing maritime radar system accuracy, particularly in adverse weather conditions, and paving the way for future research in refining environmental impact models on radar signals.

Keywords: radar signal behavior; maritime environments; falling rain; wind; ocean surface roughness

Citation: Wang, X.; Wei, M.; Wang, Y.; Sun, H.; Ma, J. Radar Signal Behavior in Maritime Environments: Falling Rain Effects. *Electronics* **2024**, *13*, 58. https://doi.org/10.3390/electronics13010058

Academic Editors: Toshifumi Moriyama and Yide Wang

Received: 13 November 2023
Revised: 17 December 2023
Accepted: 20 December 2023
Published: 21 December 2023

1. Introduction

The maritime domain stands as a critical linchpin of global trade, security, and environmental monitoring, serving as the connective tissue of nations and the lifeblood of our planet [1,2]. Within this intricate tapestry of maritime activities, radar technology assumes a paramount role in navigation, surveillance, and environmental assessment [3]. Maritime radionavigation radar systems are indispensable for ensuring vessel safety, monitoring dynamic oceanic conditions, and countering threats such as piracy and illicit trafficking. These radar systems, integral to the maritime ecosystem, rely heavily on precise channel modeling for accurate calibration [4–6]. A robust channel model provides essential calibration references, enabling radar systems to navigate with precision, track targets, and operate reliably, even in adverse weather conditions [7]. This calibration is of paramount importance for vessels of all sizes, from colossal oil tankers to passenger ships and container carriers, plying our vast oceans.

In fair weather conditions, radar signals primarily interact with the ocean surface through the scattering of electromagnetic waves by wind-generated gravity and capillary waves [8,9]. A study investigated the relationship between X-band Doppler radar signals and wind components over the ocean surface, employing the Grassburger–Procaccia algorithm [10]. It highlighted a close correlation between radar reflectivity and surface winds. However, during adverse weather conditions, radar signal interactions become intricate. Recent studies in the field of radar signal interaction with the ocean surface in different weather conditions have also explored the complex interplay of air–sea interactions, particularly during severe atmospheric and oceanic events [11–13]. These investigations delve into the dynamic feedback mechanisms between the atmosphere and ocean, spanning a wide range of spatial and temporal scales.

Falling raindrops introduce a myriad of effects on radar signals, including absorption, scattering, and backscattering, resulting in unpredictable behaviors [14]. However, knowledge about oceanic rainfall is poor due to numerous technical difficulties in the measurement of this fast-changing phenomenon, such as the fact that ground-based radar has a limited range, and gauges on islands or buoys can only give scattered readings [15]. When raindrops hit the ocean surface, they create complex features like ring waves, splashes, and secondary droplets. These phenomena have been extensively studied in references [16,17], which revealed that individual raindrops generate ring waves with wavelengths of 1–2 cm, observable in areas up to 50 cm in diameter. Investigations using rain simulators and capacitance probes have provided detailed insights into the nature of these waves and their impact on radar backscattering, by finding specific spectral characteristics of the waves [18,19]. Additionally, ocean surface waves, crucial for radar signatures, are influenced by rainfall through momentum exchange, as shown in the theoretical analysis in reference [20]. Experiments by Tsimplis et al. demonstrated the rain's effect on wave dynamics, including damping of larger gravity waves and enhancement of smaller capillary waves [21]. Contreras et al. developed a numerical model to further understand these interactions and their effects on microwave backscatter [22].

It is typical that convective rain cells over oceans are seen as bright patterns with sharp edges and a dark center in Synthetic Aperture Radar (SAR) images [23–25]. This phenomenon is understood as the result of cool downdrafts from rain, generating horizontal winds and consequently surface waves detectable by radar [26,27]. The dark patches at the centers of these cells are thought to be caused by rain-induced turbulence dampening the surface waves. The exact nature of these formations, particularly for X-band radar, is still debated. Studies using SIR-C/X-SAR imagery showed a strong frequency dependence of radar backscattering from these rain cells [28,29]. This observation suggests a need for further theoretical investigation to quantitatively explain this frequency dependence, indicating that current theories may require refinement or expansion.

In response to this critical knowledge gap, this research embarks on a comprehensive exploration of the influence of falling rain on ocean surface backscattering. This work strives to advance our understanding of radar signal behavior in maritime environments, particularly in the presence of falling rain. By integrating advanced theoretical models and conducting in-depth analysis, we aim to offer practical insights that will enhance the reliability and accuracy of maritime radar systems, ultimately contributing to safer and more efficient maritime operations. The structure of this paper is as follows: Section 2 details the theoretical model developed to examine the influence of falling rain on ocean surface backscattering. Section 3 delves into channel modeling and analysis, shedding light on the intricate interplay of operating frequency, rain rate, and wind speed in radar signal propagation. Finally, Section 4 provides comprehensive conclusions, encapsulating the significance and implications of our research and outlining directions for future investigations.

2. Theoretical Model Design

Maritime mobile radar systems, operating within frequency bands of 2900–3100 MHz, 5470–5650 MHz, 8850–9000 MHz, and 9200–9500 MHz, are pivotal instruments for ensuring safe and reliable maritime navigation, as well as precise weather monitoring [30]. It has been demonstrated that the S-band is heavily encumbered by shipborne, airborne, and ground-based military radar systems in the U.S. [31] due to its less susceptibility to atmospheric attenuation. The 5 GHz band has been proven to have good potential for military applications [32], such as off-shore anti-terrorist surveillance or the application of unmanned surface vehicles (USVs) in the maritime environment. And the X-band is preferred for a sharper image and better resolution [33].

In this study, we focus our theoretical investigations on radar signals at frequencies of 3, 5, and 9 GHz. Based on the schematic representation depicted in Figure 1, the theoretical model is constructed by segmenting it into five fundamental components, each playing a distinct role in shaping radar signal propagation: (1) absorption, which can be caused by various factors, including the composition of the atmosphere or water, and it results in a decrease in the energy of the radar signal; (2) scattering, which occurs when the radar wave encounters raindrop particles that affect the direction and intensity of the radar signal; (3) backscattering induced by falling rain; (4) gaseous absorption, referring to the radar signal being absorbed by gases in the atmosphere; (5) backscattering arising from interactions with the ocean surface, which is influenced by factors like the sea state (e.g., wave height and wave direction), surface winds, and the surface roughness of the ocean. This component is particularly important in marine radar systems for navigation and oceanographic studies.

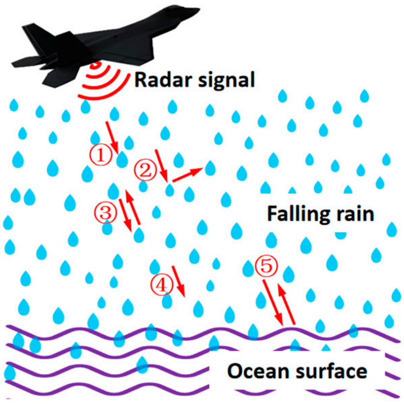

Figure 1. Diagram of effects suffered by radar signal. ① scattering, ② absorption, ③ backscattering by falling rain, ④ gaseous absorption, and ⑤ backscattering by ocean surface.

2.1. Scattering by Falling Rain

Rainfall results from the precipitation of atmospheric water vapor, leading to the formation of raindrops with varying shapes and sizes [34]. Raindrops with diameters larger than 2 mm experience pressure differences, causing them to adopt oblate spherical shapes [35,36]. To comprehensively understand the impact of falling rain on radar signal propagation, we explore two distinct scattering mechanisms: Rayleigh and Mie scattering [37,38]. Rayleigh scattering predominates when rain droplet sizes are smaller than the signal wavelength, while Mie scattering dominates when droplet sizes are comparable to or larger than the wavelength [39]. Given the typical operating frequencies of maritime mobile radar systems, we employ Rayleigh scattering theory, justified by the relatively small size of rain droplets, compared to the signal wavelength, typically ranging from sub-millimeter to approximately 7 mm with χ defined as $\chi = 2\pi r/\lambda$. Here, r is the radius of spherical raindrops, and λ is the wavelength. The expressions for scattering, backscattering, and absorption efficiencies are as follows, retaining only the most significant terms of the series expansion of Mie scattering coefficients [40]:

$$\xi_s = \frac{8}{3}\chi^4|K|^2 + \cdots \tag{1}$$

$$\xi_a = 4\chi\mathrm{Im}\{-K\} \tag{2}$$

$$\xi_b = 4\chi^4|K|^2 \tag{3}$$

where K is associated with the complex refractive index n as $K = (n^2 - 1)/(n^2 + 2)$. The refractive index, a critical dielectric property, is determined using the double-Debye dielectric model (D3M) [41], renowned for its accuracy and extensive use in deriving the dielectric constants of pure water and saline water. The real part is given by

$$\varepsilon'_w = \varepsilon_{w\infty} + \frac{\varepsilon_{w0} - \varepsilon_{w1}}{1 + (2\pi f \tau_{w1})^2} + \frac{\varepsilon_{w0} - \varepsilon_{w\infty}}{1 + (2\pi f \tau_{w2})^2} \tag{4}$$

where ε_0 refers to the permittivity of free space. It contains two relaxation terms with the corresponding relaxation time constants τ_{w1} and τ_{w2}, which implies that the imaginary part, expressed as

$$\varepsilon''_w = \frac{2\pi f \tau_{w1}(\varepsilon_{w0} - \varepsilon_{w1})}{1+(2\pi f \tau_{w1})^2} + \frac{2\pi f \tau_{w2}(\varepsilon_{w0} - \varepsilon_{w\infty})}{1+(2\pi f \tau_{w2})^2} + \frac{\sigma_i}{2\pi \varepsilon_0 f} \quad (5)$$

would exhibit maxima at both relaxation frequencies $f_{01} = 1/(2\pi\tau_{w1})$ and $f_{02} = 1/(2\pi\tau_{w2})$. The imaginary part also includes a term proportional to the ionic conductivity σ_i of the water solution when it contains dissolved salts, which could be $\sigma_i = 0$ for pure water. The other parameter functions can be found in reference [40]. This semiempirical model predicts the dielectric constant of seawater to be around 3% over the frequency range below 105 GHz [41].

Raindrop size distribution can be influenced by various microphysical and dynamic processes within and below cloud layers. In practical applications, empirical mathematical formulas derived from observed size spectra have been used to approximate natural rain size distributions. Raindrops typically follow exponential [42,43], Gamma [44], and log-normal distributions [45] in currently published investigations. The Marshall–Palmer (M-P) distribution [42] is a typical exponential function, expressed as $N(r) = N_0 \cdot e^{-\Lambda r}$, where N is the number of rain droplets of radius r + dr in a unit volume. Parameter r represents the radius of rain droplets, and parameters $N_0 = 16 \times 10^3$ [m^{-3}·mm^{-1}] and $\Lambda = 8.2Rr^{-0.21}$ [mm^{-1}] can be retrieved from rain rate Rr in mm/h [46].

The detailed calculations illustrated in Figure 2 provide a nuanced insight into the interaction between radar signals and atmospheric conditions, particularly focusing on absorption and scattering losses. The analysis reveals that absorption losses slightly outweigh scattering losses, a trend that remains consistent across a range of high frequencies extending up to the sub-terahertz domain [47]. In the context of radar systems operating at frequencies below 10 GHz and covering distances shorter than 100 km, both absorption and scattering losses appear to be minimal. This suggests that, under these specific conditions, the impact of falling rain on radar signal propagation is relatively insignificant. However, as the frequency increases beyond this threshold, the influence of both absorption and scattering on the radar signal becomes increasingly pronounced.

A particularly interesting observation from the figure is the relationship between backscattering and scattering losses. The analysis shows that backscattering induced by falling rain is comparable to scattering losses. This indicates that a considerable portion of the energy lost due to scattering is actually redirected back toward the radar system, contributing to the backscattered signal. This phenomenon is largely attributed to the omnidirectional nature of Rayleigh scattering, which, unlike other scattering mechanisms, does not exhibit a pronounced forward lobe. Consequently, in scenarios involving long distances, high-frequency operations, or heavy rain conditions, backscattering becomes a critical factor for accurate radionavigation modeling.

Furthermore, it is noteworthy to mention that an increase in rainrate correlates with an increase in backscattering. This suggests that more intense rainfall leads to a greater proportion of the radar signal being reflected back to the source. However, it is important to consider that rising absorption losses, concurrent with increased rainrates, might counteract this effect by reducing the overall intensity of backscattering that is detectable by radar systems. This complex interplay between rainrate, absorption, and backscattering underscores the need for a dynamic approach to radar modeling, especially in environments characterized by variable weather conditions. This aspect, along with the implications of changing atmospheric conditions on radar signal propagation, will be explored in greater depth in subsequent sections, aiming to refine the understanding of these intricate interactions and enhance the accuracy of radar-based navigation and observation systems.

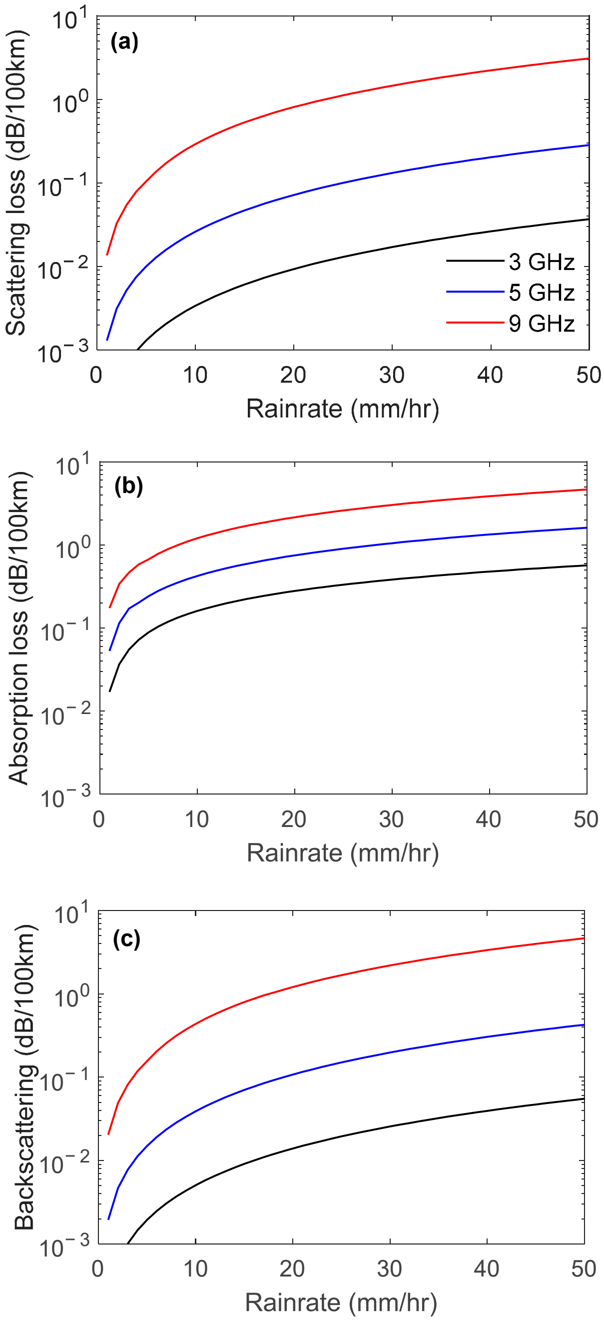

Figure 2. Degradation of radar signal due to falling rain in Mashall–Palmer drop size distribution. (**a**) Scattering loss, (**b**) absorption loss, and (**c**) backscattering by rain droplets. Plot (**b**) and (**c**) keep the same legend as plot (**a**).

2.2. Gaseous Absorption

According to reference [40], the principal sea-level atmospheric compositions consist of molecular nitrogen (N_2) and molecular oxygen (O_2) when devoid of water vapor. These gases, although transparent to visible light, interact with radio-frequency signals, playing a crucial role in radar signal propagation. The amount of water vapor present in the atmosphere is a function of several weather parameters, with particular dependence on atmospheric temperature. At sea level, the water vapor density (ρ_{wv}) can vary from as little as 10^{-2} g/m^3 in very cold, dry climates to as much as 30 g/m^3 in hot, humid climates. This variability in water vapor is significant as water vapor, alongside oxygen, exhibits substantial effects on the propagation of radio-frequency signals, especially in maritime environments where humidity levels can vary greatly. Thus, the gaseous absorption coefficient κ_g can be calculated using the sum of the oxygen absorption coefficient κ_{O_2} and the water vapor absorption coefficient κ_{H_2O}. These coefficients are derived from the Modified Power Model (MPM), as documented in reference [48]:

$$\kappa_g = \kappa_{O_2} + \kappa_{H_2O} \tag{6}$$

where the oxygen absorption coefficient $\kappa_{O_2} = 0.182 f N''_{O_2}$ includes the summation of 44 oxygen spectral lines, each of which has tails that extend over the entire electromagnetic spectrum. The water vapor absorption coefficient $\kappa_{H_2O} = 0.182 f N''_{H_2O}$ sums 34 water vapor lines and the equivalent line representing the continuum above 1 THz. The line strengths and line widths are functions of the ambient temperature T, barometric pressure P, and partial pressure of water vapor P_{H_2O}. A commonly used theoretical model, provided by the ITU Recommendation Sector (ITU-R) [49,50], accounts for gaseous absorption based on the MPM model. ITU-R also provides a prediction model for rain attenuation using the equation $\alpha_{\text{rain}} = kRr^{a}$, with the values of a and k determined for a given frequency in the range of 1 GHz to 1 THz, based on fitting measurement data.

We calculate gaseous attenuation concerning relative humidity under standard pressure (1013 mbar) and temperature (20 °C) conditions, representing typical outdoor conditions. Our results, as illustrated in Figure 3, indicate that gaseous attenuation becomes particularly severe for 9 GHz signals when the relative humidity exceeds 20%. This significant finding highlights that as operating frequencies increase, the role of gaseous attenuation becomes increasingly critical, dominating the limitations on long-distance signal transmission. This effect is especially pronounced in the terahertz frequency range, where higher frequencies interact more intensely with atmospheric gases [51].

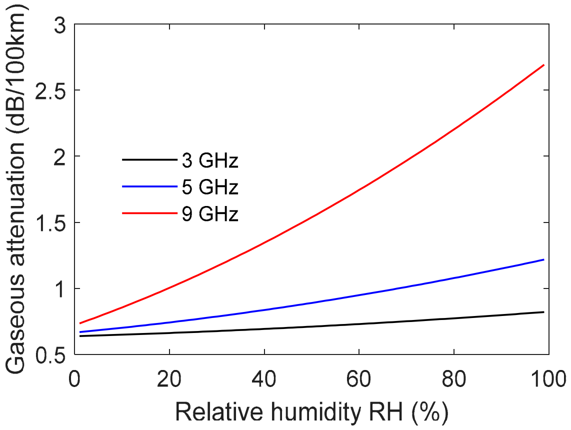

Figure 3. Attenuation due to atmospheric gases versus relative humidity under different frequencies.

2.3. *Backscattering by Ocean Surface*

Characterizing ocean surface roughness relies on two fundamental parameters: the standard deviation of the surface height variation (*rms* height) σ, providing insights into the vertical roughness of the surface, and the surface correlation length L_c, indicating the correlation between adjacent height points [52]. Additionally, the *rms* slope parameter, denoted as m, allows for an assessment of the relative contribution of multiple scattering effects. Surface smoothness is traditionally evaluated using the Rayleigh roughness criterion, which serves as a first-order indicator of surface roughness. However, a more stringent criterion, known as the Fraunhofer criterion and introduced by Ulaby [53], defines a smooth surface when the phase difference $\Delta\phi$ is less than $\pi/8$. This condition corresponds to σ being smaller than $\lambda/(32\cos\theta_i)$ for a random surface, a criterion particularly relevant in the frequency range of 3–9 GHz, where the wavelength λ is typically on the same order of magnitude as the *rms* height σ of the ocean surface.

It is worth noting that the challenge of solving the scattering problem of electromagnetic waves remains unsolved, with no exact closed-form solutions available to date. Nonetheless, the scientific community has made numerous efforts to investigate and comprehend these scattering effects. Rigorous numerical simulation techniques, including the method of moments (MoM) [54], finite-difference time-domain (FDTD) [55], and time-domain integral equation methods [56], have been employed to address the scattering problem associated with random rough surfaces. However, it is important to acknowledge that these techniques, while valuable, are computationally intensive and demand a meticulous description of the simulation scenario, which can impact result accuracy. An alternative approach is the Effective Roughness model, which incorporates the Lambertian model and directive scattering model to describe radiation patterns resulting from scattering [57,58]. However, this model relies solely on RMS height for characterizing surface roughness. Another model, the Beckman–Kirchhoff model, considers both RMS height and correlation length but assumes a Gaussian distribution for surface height [58,59]. While this model is effective for many target scenarios, it may not be suitable for all situations.

In this work, we adopt the modified integral equation model (IEM), a widely recognized and extensively utilized theory for modeling diffuse scattering, particularly relevant in the context of maritime environments [52,60–63]. The IEM is distinguished for its ability to compute the emissivity of a rough surface. It achieves this by intricately integrating the total bistatic scattering across the entire upper hemisphere. This approach is particularly effective in capturing the complex interactions of electromagnetic waves with uneven surfaces such as the ocean. The model employs a sophisticated system of four distinct correlation functions, each contributing to a multi-layered representation of the surface height profile. This layered approach allows the IEM to accurately characterize a range of roughness scales, offering it a broader scope of application and greater accuracy compared to traditional models like the small perturbation and Kirchhoff scattering models.

For analyzing the backscattering phenomenon originating from the sea surface, a pivotal aspect of radar signal behavior in maritime environments, we divide the ocean surface field into two main components: the Kirchhoff field and the complementary field. The formulation of the backscattering coefficients in the IEM model is a complex process that can be summarized using the following equation:

$$\sigma^0_{qq} = \frac{k^2}{2}\exp\left[-2k^2s^2\cos^2\theta\right]\sum_{n=1}^{\infty}\frac{\left|I^n_{pp}\right|^2}{n!}W^{(n)} \tag{7}$$

Here, θ represents the incidence angle, directly corresponding to the angle of backscattering, which is a critical factor in determining how radar waves interact with the ocean surface. The parameter s signifies the measure of surface roughness. Typically it is derived from measured surface roughness distribution [64], but such data were not available for this study. $W^{(n)}$ symbolizes the roughness spectrum of the surface, intricately linked with the nth power of the surface correlation function, often referred to as the correlation length. This function plays a crucial role in understanding the interaction of radar waves with surface irregularities. The term I^n_{pp} in the equation is defined as follows:

$$I^n_{pp} = (2k\cos\theta)^n f_{pp}\exp\left[-k^2s^2\cos^2\theta\right] + \frac{(k\cos\theta)^n}{2}F_{pp} \tag{8}$$

where f_{pp} is related to the Kirchoff field with $f_{vv} = 2\rho_v/\cos\theta$ and $f_{hh} = -2\rho_h/\cos\theta$. ρ_v and ρ_h are the Fresnel reflection coefficients. The parameter F_{pp} is decided by the compensating field and can be expressed as

$$F_{vv} = \frac{2\sin^2\theta}{\cos\theta}\left[\left(1-\frac{\varepsilon\cos^2\theta}{\varepsilon-\sin^2\theta}\right)(1-\rho_v)^2 + \left(1-\frac{1}{\varepsilon}\right)(1+\rho_v)^2\right] \tag{9}$$

$$F_{hh} = \frac{2\sin^2\theta}{\cos\theta}\left[4\rho_h - \left(1 - \frac{1}{\varepsilon}\right)(1+\rho_h)^2\right] \quad (10)$$

However, it is important to note that Equation (7) does not account for the skewness of the surface height distribution. Skewness is a measure of the asymmetry in the height distribution of the ocean surface, and its absence in the equation means the model may not fully capture certain complexities of ocean surface scattering, particularly at low incidence angles and for rough seas [65]. For our study, we limit our investigation to low wind speeds below 7 m/s and the presence of swell, which tends to reduce the asymmetry feature of radar backscatter [66]. This limitation allows us to focus on the more predominant features of maritime backscattering while acknowledging the need for further research to incorporate the effects of skewness in future models.

To adapt the IEM model to our specific conditions, we introduce an expression for root mean square (*rms*) height as $s^2 = w_0 + w_1 \log 10(v)$, where v symbolizes wind speed. The parameters w_0 and w_1 assume empirical values tailored to the particular ocean surface under consideration. Figure 4 presents our estimation of the backscattering coefficient for a 9.6 GHz radar signal, with a correlation length (l) set at l = 16 cm. Notably, the backscattering coefficient significantly diminishes with larger incidence angles for both vertical (v-) and horizontal (h-) polarizations. Our calculations align closely with measured data obtained from a 9.6 GHz ER-2 Doppler Radar (EDOP) operating over the ocean surface in the southern Florida offshore region [67] with wind speed v = 3 m/s and parameters w_0 = 0.0009, w_1 = 0.0276. This agreement highlights the efficacy of the IEM model in predicting ocean surface backscattering, outperforming the modified Fresnel reflection equation proposed in [67].

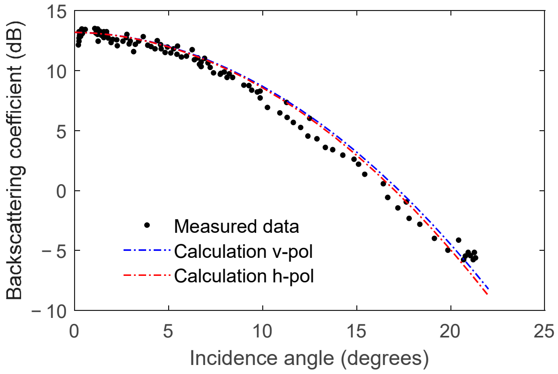

Figure 4. Measured and calculated backscattering coefficient by ocean surface. Measure data source: [43].

3. Channel Modeling and Results Analysis

In this section, we delve into the channel modeling and analysis aspect, encompassing a holistic evaluation of the radar signal behavior within the maritime environment. Our analysis takes into account all five crucial components elucidated in Figure 1, thus providing a comprehensive understanding of the intricate interplay of factors affecting radar performance in maritime scenarios. We emphasize that our study focuses primarily on the channel itself, deliberately excluding considerations of free-space path loss to concentrate on the more subtle and intricate aspects of signal behavior under specific maritime conditions. We set the wind speeds to less than 6 m/s and rain rates above 10 mm/h, conditions under which the surface features induced by rain have dominant effects on radar backscattering [6]. This choice allows us to isolate and examine the specific impacts of these environmental factors on radar signal propagation.

To initiate our analysis, it is paramount to highlight the critical influence of operating frequency on radar signal behavior. As illustrated in Figure 5a, we present a variation in backscattering concerning different operating frequencies. This comprehensive study underscores the pivotal role of frequency in shaping radar signal characteristics. A discernible trend emerges, wherein higher frequencies exhibit a substantial reduction in backscattered signal strength. This phenomenon arises due to the heightened atmospheric attenuation encountered at higher frequencies, as corroborated by previous research [46,68]. The observed effects of gaseous attenuation become particularly pronounced for channel distances exceeding 100 km, signifying that long-distance radar operations in maritime environments may require adjustments in frequency settings to optimize performance.

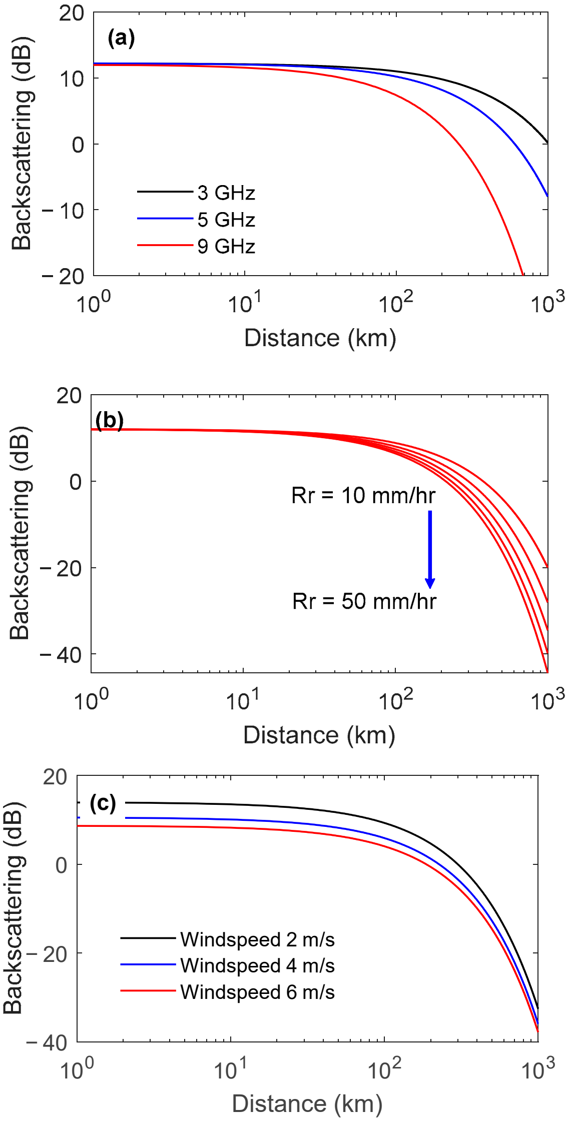

Figure 5. Variation in backscattering with respect to channel distance under different (**a**) operating frequency, (**b**) rainrate, and (**c**) wind speed with parameters relative humidity RH = 90%, incidence angle $\theta = 5^\circ$, rainrate $Rr = 30$ mm/h, and wind speed $v = 3$ m/s.

Shifting our focus to the influence of falling rain on radar signal propagation, we quantify this factor by rainrate, represented as Rr. Figure 5b illustrates the impact of varying rainrates on radar signal propagation in a clear and quantifiable manner. While the influence of rainrate is discernible, its effects appear less pronounced when compared to the dominant role played by gaseous absorption. However, our comprehensive analysis demonstrates that rain-induced effects become increasingly prominent with higher rainrates, a finding that has been validated by measured data using a C band ASAR radar [15]. This observation underscores the importance of considering the interplay of factors, including rainrate, in radar modeling, particularly in regions characterized by heavy rainfall. The data reveal that radar backscattering tends to decrease with an increase in rainrate, a phenomenon that can be attributed to the growing absorption loss induced by falling rain, rather than solely to the physical changes on the water surface in rain fields, as previously assumed [15].

Continuing our exploration, we investigate the influence of wind speed, a parameter that directly modulates ocean surface roughness. This examination sheds light on how changing wind conditions impact radar backscattering. Figure 5c portrays the variations in backscattering with respect to different wind speeds below 7 m/s, acknowledging that wind-induced surface scattering becomes more significant than rain-related scattering for wind speeds above 7 m/s [6]. The data reveal a complex relationship between wind speed and backscattering, with disparities in backscattering diminishing as channel distances increase. This intriguing observation can be attributed to the increasing prominence of gaseous and rain-induced absorption effects with greater channel distances, coupled with the relatively distance-independent nature of ocean surface roughness. Additionally, it should be noted that an increase in rainrate is occasionally accompanied by an increase in wind speed, adding to the complexity of the sea conditions. Consequently, the variations in sea conditions induced by changes in wind speed should be considered as an integral component in explaining the impact of rainfall on sea surface scattering, thereby providing a more nuanced understanding of the dynamic interplay between environmental conditions and radar signal behavior in maritime settings.

4. Conclusions

This work has systematically examined the multifaceted impact of falling rain on radar signal behavior in maritime environments, with a particular emphasis on the interplay of rain, wind, and atmospheric conditions. The findings include the significant attenuation and intricate backscattering of radar signals due to rainfall, particularly pronounced over extended channel distances. A notable frequency-dependent effect was observed, with higher frequencies showing a marked decrease in backscattered signal strength due to increased atmospheric attenuation.

The theoretical analysis, integrating all five components detailed in Figure 1, reveals the complex relationship between radar performance and environmental factors. The operating frequency plays a crucial role, with higher frequencies encountering more substantial attenuation. Falling rain, quantified by rainrate, impacts radar signal propagation with effects becoming more evident at higher rainrates. This is crucial in regions with heavy rainfall, as confirmed by C band ASAR radar data. However, these rain-induced effects are often overshadowed by the dominant impact of gaseous absorption.

Wind speed, influencing ocean surface roughness, also significantly impacts radar backscattering. This work, focusing on wind speeds below 7 m/s, shows that variations in sea conditions due to wind changes are integral in understanding rainfall's impact on sea surface scattering. However, the disparities in backscattering decrease as channel distances increase, attributed to the growing importance of gaseous and rain-induced absorption.

Despite these insights, this work has limitations. The theoretical model primarily addresses specific frequency ranges and environmental conditions, potentially overlooking the complexities of highly dynamic maritime environments. Future research should aim to extend the model's applicability to broader conditions and further explore the nuanced interactions between environmental factors and radar signals. This would enhance the precision of radar systems in maritime navigation and weather monitoring, contributing significantly to maritime safety and operational efficiency.

Author Contributions: Conceptualization, X.W. and J.M.; methodology, X.W., M.W. and J.M.; software, X.W. and M.W.; validation, H.S. and J.M.; formal analysis, X.W. and J.M.; investigation, X.W. and M.W.; resources, J.M.; data curation, X.W. and M.W.; writing—original draft preparation, X.W., M.W. and J.M.; writing—review and editing, M.W. and J.M.; visualization, M.W. and Y.W.; supervision, H.S. and J.M.; project administration, J.M.; funding acquisition, J.M. All authors have read and agreed to the published version of the manuscript.

Funding: This research was supported in part by the National Natural Science Foundation of China (62071046), the Graduate Innovative Practice Project of Tangshan Research Institute, BIT (TSDZXX202201), the Science and Technology Innovation Program of Beijing Institute of Technology (2022CX01023), and the Talent Support Program of Beijing Institute of Technology "Special Young Scholars" (3050011182153).

Data Availability Statement: Data is contained within the article.

Conflicts of Interest: Author Ying Wang was employed by the company Lenovo (Beijing) Information Technology Corporation Ltd. The remaining authors declare that the research was conducted in the absence of any commercial or financial relationships that could be construed as a potential conflict of interest.

References

1. Cordner, L. Rethinking maritime security in the Indian Ocean Region. *J. Indian Ocean Reg.* **2010**, *6*, 67–85. [CrossRef]
2. Biden, J. *National Security Strategy*; The White House: Washington, DC, USA, 2022.
3. Pope, A.; Wagner, P.; Johnson, R.; Shutler, J.D.; Baeseman, J.; Newman, L. Community review of Southern Ocean satellite data needs. *Antarct. Sci.* **2017**, *29*, 97–138. [CrossRef]
4. Leinonen, J.; Szyrmer, W. Radar signatures of snowflake riming: A modeling study. *Earth Space Sci.* **2015**, *2*, 346–358. [CrossRef] [PubMed]
5. Liu, X.; Zheng, Q.; Liu, R.; Sletten, M.A.; Duncan, J.H. A Model of Radar Backscatter of Rain-Generated Stalks on the Ocean Surface. *IEEE Trans. Geosci. Remote* **2017**, *55*, 767–776. [CrossRef]
6. Xu, F.; Li, X.; Wang, P.; Yang, J.; Pichel, W.G.; Jin, Y. A Backscattering Model of Rainfall Over Rough Sea Surface for Synthetic Aperture Radar. *IEEE Trans. Geosci. Remote* **2015**, *53*, 3042–3054. [CrossRef]
7. Liu, M.; Zhang, Z.; Chen, Y.; Ge, J.; Zhao, N. Adversarial Attack and Defense on Deep Learning for Air Transportation Communication Jamming. *IEEE Trans. Intell. Transp.* **2023**, 1–14. [CrossRef]
8. Huehnerfuss, H.; Alpers, W.; Cross, A.; Garrett, W.D.; Keller, W.C.; Plant, W.J.; Schuler, D.L.; Lange, P.A.; Schlude, F. The modification of X and L band radar signals by monomolecular sea slicks. *J. Geophys. Res.* **1983**, *88*, 9817–9822. [CrossRef]
9. Phillips, O.M. Radar returns from the sea surface—Bragg scattering and breaking waves. *J. Phys. Oceanogr.* **1988**, *18*, 1065–1074. [CrossRef]
10. Palmer, A.J.; Kropfli, R.A.; Fairall, C.W. Signatures of deterministic chaos in radar sea clutter and ocean surface winds. *Chaos Interdiscip. J. Nonlinear Sci.* **1995**, *5*, 613–616. [CrossRef]
11. Jayasinghe, A.; Elliott, S.; Gibson, G.A.; Vandemark, D. The Role of Phytoplankton Biomacromolecules in Controlling Ocean Surface Roughness. *Atmosphere* **2022**, *13*, 2101. [CrossRef]
12. Prakash, K.R.; Pant, V.; Udaya Bhaskar, T.V.S.; Chandra, N. What Made the Sustained Intensification of Tropical Cyclone Fani in the Bay of Bengal? An Investigation Using Coupled Atmosphere–Ocean Model. *Atmosphere* **2022**, *13*, 535. [CrossRef]
13. Kwon, K.; Choi, B.; Myoung, S.; Sim, H. Propagation of a Meteotsunami from the Yellow Sea to the Korea Strait in April 2019. *Atmosphere* **2021**, *12*, 1083. [CrossRef]
14. Ulaby, F.T.; Long, D.G. *Microwave Radar and Radiometric Remote Sensing*; University of Michigan Press: Ann Arbor, MI, USA, 2013.
15. Liu, X.; Zheng, Q.; Liu, R.; Wang, D.; Duncan, J.H.; Huang, S.J. A study of radar backscattering from water surface in response to rainfall. *J. Geophys. Res. Oceans* **2016**, *121*, 1546–1562. [CrossRef]
16. Fedorchenko, A.I.; Wang, A. On some common features of drop impact on liquid surfaces. *Phys. Fluids* **2004**, *16*, 1349–1365. [CrossRef]
17. Le Méhauté, B. Gravity-capillary rings generated by water drops. *J. Fluid Mech.* **1988**, *197*, 415–427. [CrossRef]
18. Bliven, L.F.; Sobieski, P.W.; Craeye, C. Rain generated ring-waves: Measurements and modelling for remote sensing. *Int. J. Remote Sens.* **1997**, *18*, 221–228. [CrossRef]
19. Lemaire, D.; Bliven, L.F.; Craeye, C.; Sobieski, P. Drop size effects on rain-generated ring-waves with a view to remote sensing applications. *Int. J. Remote Sens.* **2002**, *23*, 2345–2357. [CrossRef]
20. Le Méhauté, B.; Khangaonkar, T. Dynamic interaction of intense rain with water waves. *J. Phys. Oceanogr.* **1990**, *20*, 1805–1812. [CrossRef]
21. Tsimplis, M.; Thorpe, S.A. Wave damping by rain. *Nature* **1989**, *342*, 893–895. [CrossRef]
22. Contreras, R.F.; Plant, W.J. Surface effect of rain on microwave backscatter from the ocean: Measurements and modeling. *J. Geophys. Res. Oceans* **2006**, *111*. [CrossRef]
23. Jackson, C.R.; Apel, J.R. *Synthetic Aperture Radar Marine User's Manual*; National Oceanic and Atmospheric Administration: Washington, DC, USA, 2004.
24. Fu, L.; Holt, B. *SEASAT Views Oceans and Sea Ice with Synthetic-Aperture Radar*; California Institute of Technology, Jet Propulsion Laboratory: Pasadena, CA, USA, 1982.
25. Melsheimer, C.; Alpers, W.; Gade, M. Simultaneous observations of rain cells over the ocean by the synthetic aperture radaraboard the ERS satellites and by surface-based weather radars. *J. Geophys. Res. Oceans* **2001**, *106*, 4665–4677. [CrossRef]
26. Atlas, D. Origin of storm footprints on the sea seen by synthetic aperture radar. *Science* **1994**, *266*, 1364–1366. [CrossRef] [PubMed]

27. Atlas, D. Footprints of storms on the sea: A view from spaceborne synthetic aperture radar. *J. Geophys. Res. Oceans* **1994**, *99*, 7961–7969. [CrossRef]
28. Melshelmer, C.; Alpers, W.; Gade, M. Investigation of multifrequency/multipolarization radar signatures of rain cells over the ocean using SIR-C/X-SAR data. In Proceedings of the IGARSS '96. 1996 International Geoscience and Remote Sensing Symposium, Lincoln, NE, USA, 31 May 1996.
29. Jameson, A.R.; Li, F.K.; Durden, S.L.; Haddad, Z.S.; Holt, B.; Fogarty, T.; Im, E.; Moore, R.K. SIR-C/X-SAR observations of rain storms. *Remote Sens. Environ.* **1997**, *59*, 267–279. [CrossRef]
30. ITU Radiocommunication Bureau. Technical Characteristics of Maritime Radionavigation Radars. Available online: https://www.itu.int/dms_pubrec/itu-r/rec/m/R-REC-M.1313-1-200005-W!!PDF-E.pdf (accessed on 10 November 2023).
31. Clegg, A.W.; Seguin, S.A.; Marks, R.J.; Baylis, C. Radar Sharing in the U.S. 3 GHz Band. In Proceedings of the 2022 IEEE Radar Conference, New York, NY, USA, 21–25 March 2022.
32. Dong, F.; Chan, C.W.; Lee, Y.H. Channel modeling in maritime environment for USV. In Proceedings of the Defence Technology Asia, Singapore, 7–8 February 2011.
33. Honegger, D.A.; Haller, M.C.; Holman, R.A. High-resolution bathymetry estimates via X-band marine radar: 1. beaches. *Coast. Eng.* **2019**, *149*, 39–48. [CrossRef]
34. Janapati, J.; Seela, B.K.; Lin, P.; Wang, P.K.; Tseng, C.; Reddy, K.K.; Hashiguchi, H.; Feng, L.; Das, S.K.; Unnikrishnan, C.K. Raindrop size distribution characteristics of Indian and Pacific Ocean tropical cyclones observed at India and Taiwan sites. *J. Meteorol. Soc. Jpn.* **2020**, *98*, 299–317. [CrossRef]
35. Pruppacher, H.R.; Beard, K.V. A wind tunnel investigation of the internal circulation and shape of water drops falling at terminal velocity in air. *Q. J. Roy. Meteor. Soc.* **1970**, *96*, 247–256. [CrossRef]
36. Pruppacher, H.R.; Pitter, R.L. A Semi-Empirical Determination of the Shape of Cloud and Rain Drops. *J. Atmos. Sci.* **1971**, *28*, 86–94. [CrossRef]
37. Lockwood, D.J. Rayleigh and Mie Scattering. In *Encyclopedia of Color Science and Technology*; Springer: New York, NY, USA, 2016.
38. Deirmendjian, D. *Electromagnetic Scattering on Spherical Polydispersions*; American Elsevier Publishing: New York, NY, USA, 1969.
39. Pruppacher, H.R.; Klett, J.D. *Microphysics of Clouds and Precipitation*; Kluwer Academic Publishers: Dordrecht, The Netherlands, 1997.
40. Ulaby, F.T.; Moore, R.K.; Fung, A.K. *Microwave Remote Sensing: Active and Passive. Volume I-Microwave Remote Sensing Fundamentals and Radiometry*; Artech House: Norwood, MA, USA, 1981.
41. Matzler, C. *Thermal Microwave Radiation: Applications for Remote Sensing*; The Institution of Engineering and Technology: Stevenage, UK, 2006.
42. Marshall, J.S.; Palmer, W.M.K. The distribution of raindrops with size. *J. Atmos. Sci.* **1948**, *5*, 165–166. [CrossRef]
43. Zhang, G.; Xue, M.; Cao, Q.; Dawson, D. Diagnosing the Intercept Parameter for Exponential Raindrop Size Distribution Based on Video Disdrometer Observations: Model Development. *J. Appl. Meteorol. Clim.* **2008**, *47*, 2983–2992. [CrossRef]
44. Wolf, D.A. On the Laws-Parsons distribution of raindrop sizes. *Radio Sci.* **2001**, *36*, 639–642. [CrossRef]
45. Cerro, C.; Codina, B.; Bech, J.; Lorente, J. Modeling Raindrop Size Distribution and Z(R) Relations in the Western Mediterranean Area. *J. Appl. Meteorol. Clim.* **1997**, *36*, 1470–1479. [CrossRef]
46. Amarasinghe, Y.; Zhang, W.; Zhang, R.; Mittleman, D.M.; Ma, J. Scattering of Terahertz Waves by Snow. *J. Infrared Millim. Terahertz Waves* **2020**, *41*, 215–224. [CrossRef]
47. Wang, R.; Mei, Y.; Meng, X.; Ma, J. Secrecy performance of terahertz wireless links in rain and snow. *Nano Commun. Netw.* **2021**, *28*, 100350. [CrossRef]
48. Liebe, H.J.; Hufford, G.A.; Cotton, M.G. Propagation modeling of moist air and suspended water/ice particles at frequencies below 1000 GHz. In Proceedings of the AGARD 52nd Specialists' Meeting of the Electromagnetic Wave Propagation Panel, Palma de Mallorca, Spain, 17–20 May 1993.
49. Recommendation ITU-R P.676-11: Attenuation by Atmospheric Gases. Available online: https://www.itu.int/dms_pubrec/itu-r/rec/p/R-REC-P.676-11-201609-I!!PDF-E.pdf (accessed on 10 November 2023).
50. International Telecommunication Union Recommendation (ITU-R) P.676-13: Attenuation by Atmospheric Gases and Related Effects. Available online: https://www.itu.int/dms_pubrec/itu-r/rec/p/R-REC-P.676-13-202208-I!!PDF-E.pdf (accessed on 10 November 2023).
51. Federici, J.F.; Ma, J.; Moeller, L. Review of weather impact on outdoor terahertz wireless communication links. *Nano Commun. Netw.* **2016**, *10*, 13–26. [CrossRef]
52. Fung, A.K. *Microwave Scattering and Emission Models and Their Applications*; Artech House: Norwood, MA, USA, 1994.
53. Ulaby, F.T.; Moore, R.K.; Fung, A.K. *Microwave Remote Sensing: Actice and Passive. Volume II-Radar Remote Sensing and Surface Scattering and Emission Theory*; Artech House: Norwood, MA, USA, 1982.
54. He, J.; Yu, T.; Geng, N.; Carin, L. Method of moments analysis of electromagnetic scattering from a general three-dimensional dielectric target embedded in a multilayered medium. *Radio Sci.* **2000**, *35*, 305–313. [CrossRef]
55. Bourgeois, J.M.; Smith, G.S. A Fully Three-Dimensional Simulation of a Ground-Penetrating Radar: FDT with Experiment Theory Compared. *IEEE Trans. Geosci. Remote* **1996**, *34*, 36–44. [CrossRef]
56. Harrington, R.F. *Field Computation by Moment Methods*; Wiley-IEEE Press: Hoboken, NJ, USA, 1993.

57. Degli-Esposti, V.; Guiducci, D.; De'Marsi, A.; Azzi, P.; Fuschini, F. An advanced field prediction model including diffuse scattering. *IEEE Trans. Antenn. Propag.* **2004**, *52*, 1717–1728. [CrossRef]
58. Beckmann, P.; Spizzichino, A. *The Scattering of Electromagnetic Waves from Rough Surfaces*; Artech House: Norwood, MA, USA, 1987.
59. Harvey, J.E.; Krywonos, A.; Vernold, C.L. Modified Beckmann-Kirchhoff scattering model for rough surfaces with large incident and scattering angles. *Opt. Eng.* **2007**, *46*, 78002–780010. [CrossRef]
60. Fung, A.K.; Li, Z.; Chen, K.S. Backscattering from a randomly rough dielectric surface. *IEEE Trans. Geosci. Remote* **1992**, *30*, 356–369. [CrossRef]
61. Fung, A.K.; Liu, W.Y.; Chen, K.S.; Tsay, M.K. An Improved Iem Model for Bistatic Scattering from Rough Surfaces. *J. Electromagn. Waves Appl.* **2002**, *16*, 689–702. [CrossRef]
62. Alvarez-Perez, J.L. An extension of the IEM/IEMM surface scattering model. *Waves Random Media* **2001**, *11*, 307–329. [CrossRef]
63. Alvarez-Perez, J.L.; Vall-Ilossera, M.; Nieto-Borge, J.C. Emissivity Calculations for two-dimensional ocean Surfaces with the improved Integral Equation Model IEM2M. In Proceedings of the 2006 IEEE International Symposium on Geoscience and Remote Sensing, Denver, CO, USA, 31 July–4 August 2006.
64. Wei, J.C.; Chen, H.; Qin, X.; Cui, T.J. Surface and Volumetric Scattering by Rough Dielectric Boundary at Terahertz Frequencies. *IEEE Trans. Antenn. Propag.* **2017**, *65*, 3154–3161. [CrossRef]
65. Voronovich, A.G.; Zavorotny, V.U. Theoretical model for scattering of radar signals in Ku-and C-bands from a rough sea surface with breaking waves. *Waves Random Media* **2001**, *11*, 247–269. [CrossRef]
66. Chu, X.; He, Y.; Chen, G. Asymmetry and Anisotropy of Microwave Backscatter at Low Incidence Angles. *IEEE Trans. Geosci. Remote* **2012**, *50*, 4014–4024. [CrossRef]
67. Li, L.; Heymsfield, G.M.; Tian, L.; Racette, P.E. Measurements of Ocean Surface Backscattering Using an Airborne 94-GHz Cloud Radar—Implication for Calibration of Airborne and Spaceborne W-Band Radars. *J. Atmos. Ocean. Technol.* **2005**, *22*, 1033–1045. [CrossRef]
68. Li, P.; Wang, J.; Zhao, L.; Ma, J.; Sun, H.; Moeller, L.; Federici, J.F. Performance degradation of terahertz channels in emulated rain. *Nano Commun. Netw.* **2023**, *35*, 100431. [CrossRef]